Nano Energy 59 (2019) 327–335

Contents lists available at ScienceDirect

Nano Energy

journal homepage: www.elsevier.com/locate/nanoen

Full paper

Insights into the structural evolution and Li/O loss in high-Ni layered oxide cathodes

Defei Kong[a], Mingjian Zhang[a,b,*], Yinguo Xiao[a], Jiangtao Hu[a], Wenguang Zhao[a], Lei Han[a], Feng Pan[a,*]

[a] School of Advanced Materials, Peking University, Shenzhen Graduate School, Shenzhen 518055, People's Republic of China
[b] Sustainable Energy Technologies Department, Brookhaven National Laboratory, Upton, NY 11973, USA

ARTICLE INFO

Keywords:
Li-ion batteries
High-Ni layered oxides
Structural evolution
Li/O loss
In-situ TEM

ABSTRACT

High-Ni layered oxides are one class of the most promising cathodes for Lithium ion batteries (LIBs) due to the high capacity and low cost. Accompanying with the high Ni content, Li/O loss from the layered structure, as well as the relevant structural evolution, have been extensively considered as a general origin for various detrimental phenomena, such as cationic disordering during high-temperature solid-state synthesis, chemical weathering at the surface during storage, and the capacity fading at high upper voltages (> 4.3 V) during electrochemical tests. Herein, multiple macroscopic/microscopic characterization techniques, including *in-situ* transmission electron microscopy (TEM), *ex-situ* X-ray diffraction (XRD), and X-ray photoelectron spectra (XPS), are combined to comprehensively investigate the thermal-induced local structural evolution *vs* Li/O loss in a representative binary high-Ni layered oxide $LiNi_{0.9}Co_{0.1}O_2$. The heterogenous Li/O loss kinetics in the bulk and at the surface are simultaneously tracked based on a rational structural model, revealing a quantitative relationship between Li/O loss and the phase transformation. The local structural evolution within single primary particles monitored by *in-situ* TEM further uncovers that, Li/O loss at the particle surface is accelerated *via* the large Li^+ diffusivity at high temperatures, finally leads to a phase transformation process from the bulk to the surface, in which a peculiar "anti-core-shell" structure within single primary particles is observed. The quantitative analysis combined with the direct observation not only demonstrate a feasible route to investigate the Li/O loss kinetics, but also provide valuable insights into the performance improvement of high-Ni layered oxides from the aspect of Li/O loss.

1. Introduction

Since rechargeable Li-ion batteries (LIBs) were first commercialized in the 1990s, continuous efforts have been devoted to developing high-energy-density LIBs. High-Ni Ni-Co-Mn (NMC, Ni content > 60%) layered oxides have been considered as one class of the most promising cathodes for next-generation Li-ion batteries due to the low cost and high capacity [1–3]. Recently, a series of high-Ni NMC cathodes, such as $LiNi_{0.7}Mn_{0.15}Co_{0.15}O_2$ [4,5], $LiNi_{0.8}Mn_{0.1}Co_{0.1}O_2$ [6–8], $LiNi_{0.9}Co_{0.07}Al_{0.03}O_2$ [9], and $LiNi_{0.95}Co_{0.025}Al_{0.025}O_2$ [10], have been reported as the high-energy-density cathodes to replace $LiCoO_2$ and low-Ni NMC cathodes for electric vehicles (EVs) and small-scale grid storage applications [11].

Nevertheless, the increase of Ni content also brings with many issues, such as the difficulty to synthesize highly-ordered materials, the poor storage property, and the inferior cycling stability [12–14]. These issues greatly block the way to implement the practical applications of high-Ni NMC cathodes. To solve these problems, the mechanism beneath these issues must be revealed and understood firstly. According to the previous reports, various detrimental phenomena during synthesis, storage and cycling are considered to be related with Li/O loss from layered oxide lattices. Wang et al. reported that, a swift Li/O loss at high temperature induced serious cationic mixing in the bulk and produced NiO-type rock-salt phase at the particle surface during synthesis of $LiNi_{0.7}Mn_{0.15}Co_{0.15}O_2$, which greatly decreased the practical capacity of high-Ni layered oxide [4,5]. Hya and You et al. reported that, chemical weathering continuously occurred at the particle surface to produce Li-containing residues (including LiOH, $LiHCO_3$ and Li_2CO_3) when storing high-Ni layered oxides in air or moist environments, which also presented a direct relationship with Li/O loss, and resulted into a similar phase transformation from layered oxides to rock-salt phase at the particle surface [15–17]. During the

* Corresponding authors.
E-mail addresses: zhangmj@pkusz.edu.cn (M. Zhang), panfeng@pkusz.edu.cn (F. Pan).

https://doi.org/10.1016/j.nanoen.2019.02.059
Received 30 November 2018; Received in revised form 19 January 2019; Accepted 22 February 2019
Available online 22 February 2019

electrochemical cycling, the low coulombic efficiency for the first cycle has been reported to be related with the surface reconstruction involving the irreversible Li/O loss during the formation of SEI membrane. Moreover, the high voltage operation (> 4.3 V) at elevated temperature, always a big issue for high-Ni layered oxides, is also extensively reported to accompany with Li/O loss in the bulk and at the surface, which not only results in a fast capacity decay [18–21], even brings with big safety concerns due to the release of highly reactive oxygen [22,23]. Therefore, in-depth understanding the local structural evolution *vs* Li/O loss will provide valuable information for new material design, current material improvement, and preventive procedure development during operations of LIBs.

Although Li/O loss has been extensively reported as a universal origin for various detrimental phenomena above, quantitative studies about how Li/O loss happens, and how much of Li/O loss can induce the phase transformation, are very rare [24,25]. It is mainly due to various technique and operation challenges: (1) the scarcity of the quantitative characterization techniques for light elements, namely Li and O here. For example, inductively coupled plasma – atomic emission spectrometry (ICP-AES), a powerful tool to determine the content of light elements, can only give a total Li content, but not distinguish which phase Li element comes from (some Li-containing residues, such as LiOH, Li_2CO_3, $LiHCO_3$, etc., always inevitably coexist with the layered phase during synthesis/storage/cycling) [26–30]; (2) the oxygen contamination from the practical operation environments, such as the synthesis of high-Ni layered oxides under O_2, the industrial storage in ambient air, and the electrochemical tests in the Li/O-containing electrolytes; (3) Li/O loss usually occurs very locally, even at the nanoscale/atomic level, such as surface reconstruction during storage and cycling; (4) the rational structural models need to be constructed to correlate the structural evolution with Li/O loss. All these challenges pose great limitations on the investigation of Li/O loss. To solve these problems, the combination of characterization techniques covering different aspects and multilength scales, ranging from the average bulk/surficial structural/chemical information for lots of particles to the local structural information at the nanosized/atomic level within single particles, is desirable.

In this work, we combine multiple macroscopic/microscopic characterization techniques, including *in-situ* transmission electron microscopy (TEM), *ex-situ* X-ray diffraction (XRD), and X-ray photoelectron spectra (XPS), to comprehensively investigate the thermal-induced local structural evolution *vs* Li/O loss in a representative binary high-Ni layered oxide $LiNi_{0.9}Co_{0.1}O_2$. The heterogenous Li/O loss kinetics in the bulk and at the surface are simultaneously tracked based on a rational structural model, which quantitatively correlate Li/O loss with the phase transformation from layered phase to rock-salt phase. The local structural evolution process within single primary particles is further monitored by *in-situ* TEM tuned in-operate at 25–900 °C. It clearly demonstrates a phase transformation from the bulk to the surface, which could be ascribed to Li/O loss at the particle surface as well as the high Li^+ diffusivity in the bulk. Such findings can shed light on the performance improvement of high-Ni layered oxides from the view of Li/O loss.

2. Results and discussions

2.1. As-prepared NC91 and the initial structural model for Li/O loss

NC91 is prepared by the traditional solid-state methods through calcining the mixture of $(Ni_{0.9}Co_{0.1})(OH)_2$ and LiOH. X-ray diffraction (XRD) pattern in Fig. 1a presents a well-defined layered structure based on α-$NaFeO_2$ with *R-3m* space group. The big ratio of the integrated intensities of (003) and (104) peaks (denoted as $I_{(003)}/I_{(104)}$ = 1.68) indicates a highly ordered layered structure [5]. The morphology of NC91 is illustrated in Fig. 1b. The primary particles present similar bulk shape with the particle size around 100–700 nm, and are not assembled into the secondary particles. In addition, the surface of the samples is observed to be slightly rough and mostly covered by the island-like particles as shown in the inset of Fig. 1b, which could be Li-containing residues (e. g. Li_2CO_3, LiOH, and $LiHCO_3$) [15,26]. The elemental uniformity was also confirmed by the TEM EDX results in Fig. S1. The electrochemical tests, including the charging/discharging profile, cycling stability, CV curve and ESI spectra, were presented in Fig. S2. As expected, Fig. S2a shows a poor cycling stability due to the high Ni content.

As mentioned above, the phase transformation process from layered phase to rock-salt phase (Fig. 1c) are usually observed during synthesis/storage/electrochemical cycling, which is adopted as a model process to investigate Li/O loss behavior here. The left panel of Fig. 1c shows an ideal layered oxide structure, wherein Li^+ ions take 3b sites in Li layers, while transition metal (TM) cations, comprising of 90% Ni and 10% Co, take 3a sites, and O anions take 6c sites. According to the previous work and the insensitivity of X-ray to Li^+ ions [4,5,27], a corresponding reasonable structural model is constructed here, namely $[Li_{1-x}Ni_x]_{3b}[Ni_{0.9-x}Co_{0.1}]_{3a}O_{2-x}$, to investigate Li/O loss during the phase transformation. In this model, several constraints are set here: (1) the sum amount of Ni and Co cations keeps as 1 in the formula; (2) to keep the atomic occupancy as 1 at 3b sites, some of Ni cations migrate from 3a to 3b sites while equal amount of Li^+ ions move out from the formula; (3) O loss accompanies with Li loss and the reduction of Ni(III) in chemical stoichiometry based on the charge balance principle. Based this model, Rietveld refinement is also performed here (Fig. 1a). The relevant structural parameters are summarized in Table S1. The low Ni (3b) value with 5.9% further confirms the highly cationic ordering in as-prepared NC91.

2.2. Tracking Li/O loss in the bulk

The phase transformation was investigated by calcining NC91 at different temperatures. To exclude the influence of external O_2/CO_2 species on Li/O loss, all calcination experiments were performed in N_2 atmosphere. Corresponding XRD patterns are presented in Fig. 2a. As we can see, no peak shift is observed below 600 °C, indicating no phase transformation. When the temperature is elevated above 600 °C, layered phase gradually transforms into a main phase NiO-type rock-salt solid solution, mixed with a trace phase, CoO-type cubic phase (marked with diamonds in Fig. 2a). Four selected regions marked by dashed line squares in Fig. 2a are enlarged in Fig. 2b to show much more details during the phase transformation. Above 600 °C, peaks all shift to low angles, indicating a lattice expansion. $(003)_L$ (L represents layered phase) peak gradually disappears, $(006)_L$ and $(102)_L$ peaks merge into $(111)_R$ peak (R represents rock-salt phase), $(104)_L$ peak evolves into $(200)_R$ peak, and $(018)_L$ and $(110)_L$ merges into $(220)_R$ peak. It is basically consistent with the TGA result (Fig. S2), wherein the onset temperature of weight loss for NC91 is around 700 °C. No new peaks involvement indicates that, the phase transformation is smooth without involving any intermediate phase. This phase transformation is similar to that occurred (from layered phase to disordered spinel phase, then to rock-salt phase) during electrochemical cycling, resulting in the capacity degradation [18,28].

To quantitatively track Li/O loss during the phase transformation, Rietveld refinements of XRD patterns at RT and above 500 °C are performed by using the above mentioned structural models $[Li_{1-x}Ni_x]_{3b}[Ni_{0.9-x}Co_{0.1}]_{3a}O_{2-x}$ and $(Li_{1-x}Ni_x)O$ $(Li_{1-x}Ni(III)_{1-x}Ni(II)_{2\times-1}O)$ for the layered phase and NiO-type rock-salt phase, respectively. To simplify the models, CoO-type cubic phase observed in the above XRD patterns is neglected. The refinement results are shown in Fig. S4 and Table S2. The ratio of lattice parameters *c/a* and the occupancy of Ni at 3b sites Ni(3b) are plotted as functions of temperature to present the evolution of Li/Ni mixing at 3b sites. As shown in Fig. 2c, the *c/a* value fast decreases, accompanying with the increase of Ni(3b) value, which indicates a Li/Ni mixing process with temperature. By 800 °C, there are

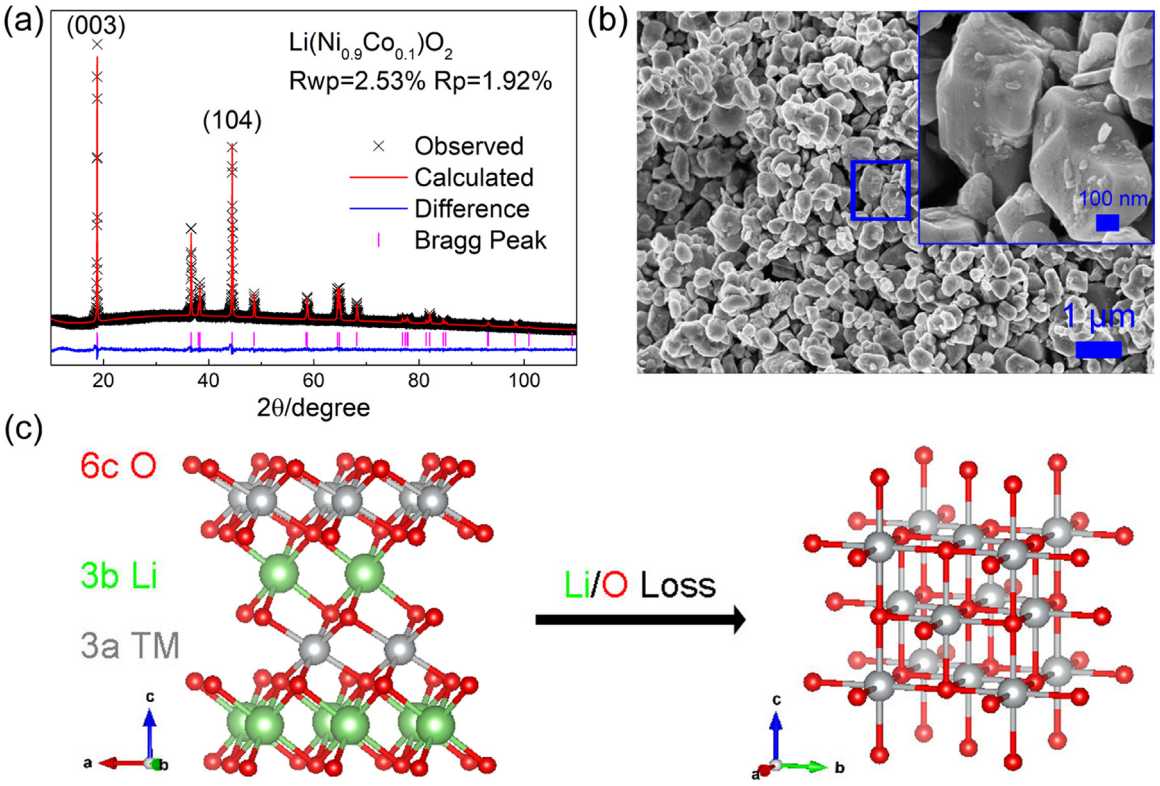

Fig. 1. As-prepared high-Ni layered oxides and the phase transformation process. (a) Experimental and calculated XRD patterns of NC91; (b) SEM image of NC91, and the inset is enlarged from the region marked by the blue rectangle; (c) Schematic illustration to show the phase transformation from layered phase to NiO-type rock-salt phase through Li/O loss.

about 30% of Ni migrating from 3a to 3b sites (Li sites), which leads a serious Li/Ni mixing in Li layers. Then an abrupt increase of Ni(3b) from 0.3 to 0.8 was observed during the phase transformation from 800 to 900 °C. Correspondingly, Li and O occupancies (denoted as Li(3b) and O(6c)) are also plotted as functions of temperature in Fig. 2d to track Li/O loss. Interestingly, Li(3b) and O(6c) values at RT are 0.95 and 0.93, respectively, indicating a slightly O-deficient layered structure with a small Li/Ni disordering. When the temperature rises to 500 °C, there is only a little Li/O loss. Then it becomes serious with the increasing temperature. When the temperature reaches at 800 °C, a great Li/O-deficient layered phase is formed with about 25% of Li loss and 20% of O loss in comparison with the initial structure at RT. When the temperature rises to 900 °C, there is about 20% Li mixing with 80% Ni in the newly-formed rock-salt phase. ICP-AES results in Table S3 indicate that, there is still much Li existed in the sample even after calcination at 900 °C, which could be attributed to lots of Li_2CO_3 residue after the phase transformation (to be discussed in next section).

In summary, there is a continuous Li/O loss during the heating treatment, leading to a Li/O-deficient layered phase with serious Li/Ni mixing below 700 °C. When the Li/O loss are larger than certain values (about 25% of Li loss and about 20% of O loss at 800 °C), the layered phase could not be preserved at high temperatures and fast transforms into rock-salt phase, which is accompanied with much more serious Li/O loss (about 50% of Li loss and 30% of O loss in comparison with the initial layered phase).

2.3. Tracking Li/O loss at the surface

The refinement results of *ex situ* XRD could only reveal the average Li/O loss in the bulk of crystalline materials. Herein, a surface characterization tool, XPS, is further used to track Li/O loss on the particle surface.

According to the previous work, Li ions extracted from the layered oxides always exist in the form of Li_2CO_3 at the particle surface [27,29–31]. So we could track Li loss by analyzing Li_2CO_3 species at the particle surface. Herein, Li_2CO_3 was formed when exposed to air during the sample transfer after the calcination in N_2 atmosphere. As shown in Fig. 3a, O 2p XPS spectra are recorded for the same samples above. The peak around 531 eV could be ascribed to metal carbonate (namely Li_2CO_3 here) or organic species containing C-O, and the other peak around 529 eV belongs to metal oxide (namely $LiNi_{0.9}Co_{0.1}O_2$ here). Accordingly, the ratio between the integrated areas of metal carbonate peak and the sum areas of two peaks (denoted as $I_{Carbonate}/I_{Carbonate+Oxide}$) can be used to represent the content percentage of metal oxides at the surface. As shown in Fig. 3b, the ratio gradually decreases below 400 °C, which could be ascribed to the decomposition of the surface organic species. It is confirmed by the little weight loss below 400 °C in TGA curve (Fig. S2). From 400 to 600 °C, the value slowly increases, hinting the slow Li loss from the oxides and the formation of Li_2CO_3 at the surface. From 600 to 700 °C, there is a big abrupt increase, indicating a fast Li loss. Above 700 °C, the value slowly decreases. It does not mean the decrease of Li loss rate, but results from the fast evaporation or decomposition of surface Li_2CO_3 species because of the low melting point of Li_2CO_3 (723 °C). In summary, Li loss from layered phase reflected by O ls XPS spectra, is basically consistent with that observed by XRD results. And It can be represented by the formula as below.

$$Li[Ni(III)_{0.9}Co(III)_{0.1}]O_2 + x/2\ CO_2 \rightarrow x/2\ Li_2CO_3 + Li_{1-x}[Ni(III)_{0.9}Co(III)_{0.1}]O_{2-x/2} \quad (1)$$

According to the discussion above, Li/O loss will lead to Li/O-deficient layered oxide $Li_{1-x}(Ni_{0.9}Co_{0.1})O_{2-x/2}$, which is instable and easy to decompose at high temperature, then results into the reduction of TM cations, mainly the reduction of Ni(IIII) here. While the reduction of Ni (III) is directly correlated with O loss in the ratio of 2: 1 to keep the charge balance as the formula below.

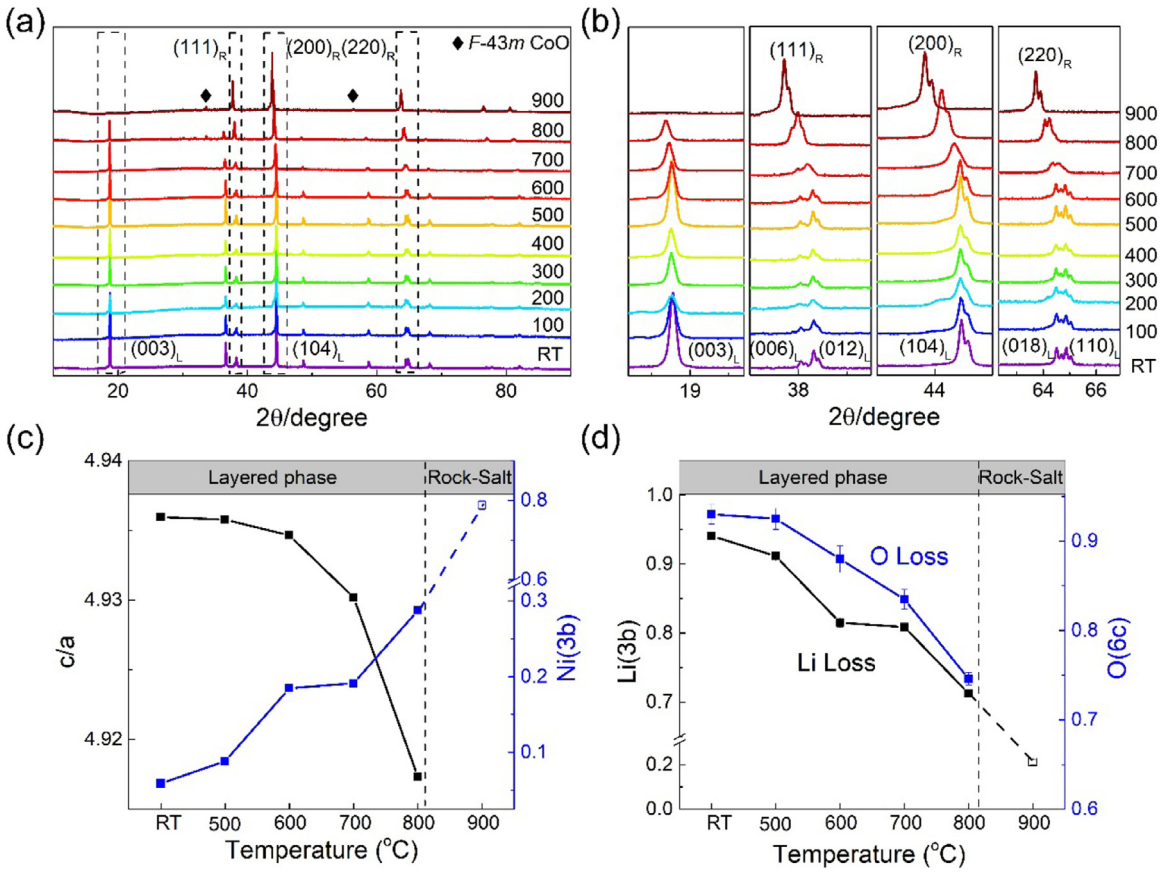

Fig. 2. Tracking Li/O loss in the bulk. (a) XRD patterns of calcined NC91 samples at different temperatures; (b) Selected regions of XRD patterns in (a); (c) (d) Refined structural parameters, including c/a, Ni(3b), Li(3b) and O(6c), as functions of temperature.

$$Li_{1-x}[Ni(III)_{0.9}Co(III)_{0.1}]O_{2-x/2} \rightarrow Li_{1-x}[Ni(III)_{0.9-y}Ni(II)_yCo(III)_{0.1}]O_{2-x/2-y/2} + y/4\ O_2 \quad (2)$$

Therefore, we could partially track O loss by monitoring the reduction of Ni(III). Ni 2p XPS spectra are recorded to study the valence change of Ni during the phase transformation here. As shown in Fig. 3c, a broad peak around 855 eV is observed, which could be splitted into two peaks. The left one at high binding energy position is for Ni(III), and the right one is for Ni(II). Peak fitting results for Ni 2p3/2 were deposited in Fig. S5. Similar with the O ls case, the ratio between the integrated areas of Ni(III) peak and the sum areas of two peaks (denoted as $I_{Ni(III)}/I_{Ni(III)+Ni(II)}$) could be used to represent the Ni(III) content at the surface. Fig. 3d presents Ni(III) content as a function of temperature. It is clear, Ni(III) content keeps constant below 300 °C, indicating no reduction of Ni(III). From 300 to 700 °C, the Ni(III) content slowly decreases, indicating a slow reduction to Ni(II) and the corresponding O loss (observed in Fig. 2d). More Ni(II) will bring with more Li/Ni mixing, which has been observed in Fig. 2c. From 700 to 900 °C, Ni(III) content undergoes a fast decrease, which corresponds to the fast phase transformation observed in the above XRD results above 700 °C. Interestingly, we could still observe 65% of Ni(III) at the surface by 900 °C, which is not consistent with the refinement result of XRD pattern at 900 °C, $(Li_{1-x}Ni_x)O$ (x = 0.8). It could be related with the microscopic Li loss process at the surface (to be discussed in the *in situ* TEM section).

By combining Formula (1) and (2) together, we could obtain the whole formula for Li/O loss as below.

$$Li[Ni(III)_{0.9}Co(III)_{0.1}]O_2 + x/2\ CO_2 \rightarrow Li_{1-x}[Ni(III)_{0.9-y}Ni(II)_yCo(III)_{0.1}]O_{2-x/2-y/2} + x/2\ Li_2CO_3 + y/4\ O_2 \quad (3)$$

It is clear, O loss during the heating process could be divided into two parts: one is accompanied with Li loss and lost in form of Li_2O, which further reacts with CO_2 to form Li_2CO_3; the other is accompanied with Ni(III) reduction and lost in form of O_2. These two parts together comprise the overall O loss behavior observed in Fig. 2d. To further take account of Li/Ni mixing, the model $Li_{1-x}[Ni(III)_{0.9-y}Ni(II)_yCo(III)_{0.1}]O_{2-x/2-y/2}$ could be simplified to $[Li_{1-x}Ni_x]_{3b}[Ni_{0.9-x}Co_{0.1}]_{3a}O_{2-x}$ by assuming x = y (namely O loss accompanied with Li loss equals to O loss accompanied with the reduction of Ni(III)), which is just the model we proposes for Rietveld refinement of XRD patterns above.

2.4. *In-situ TEM probing local structural evolution within single particles*

To get insight to how the phase transformation occurred locally, *in-situ time/temperature-resolved* TEM is used to track the local structural evolution within single particles during *in situ* calcination. Based on the XRD and XPS studies above, *in situ* TEM images are recorded at RT, 300, 500, 700 and 900 °C, respectively. Some images were selected to investigate the entire process. As shown in Fig. S6, TEM images from RT to 900 °C are presented. The single nanoparticle adjacent to the larger particle is tracked. As shown in Fig. S6h, the particle size continuously decreases with temperature/time, indicating some kinds of evaporation or decomposition processes during the calcination. The decrease of particle size from RT to 300 °C could be ascribed to the evaporation of surficial organic contamination shown in Fig. S6a, which is consistent with O 1s XPS results in Fig. 3b.

Correspondingly, fast Fourier transformation (FFT) is performed on the selected single particle in Fig. S6 to track the phase transformation process within this single particle. As shown in Fig. 4, the diffraction spots are indexed to analyze the local phase evolution process with temperature. In Fig. 4a, all the diffraction spots belong to the layered structure, and are indexed as $(104)_L$, $(006)_L$, and $(-102)_L$, which correspond to the strongest peak and a double peak in the XRD patterns

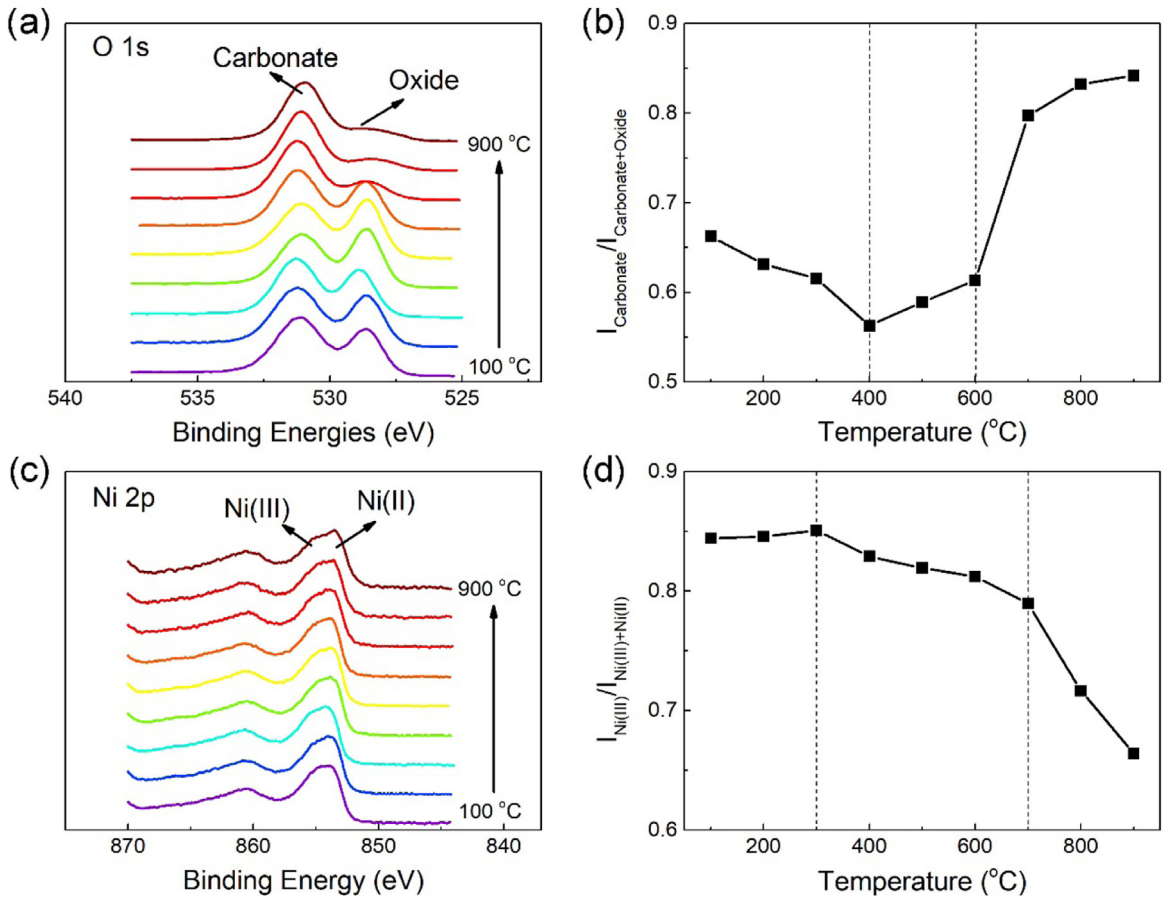

Fig. 3. Tracking Li/O loss at the surface. (a) O 1s XPS spectra for calcined NC91 samples at different temperatures; (b) The ratio of the integrated areas of oxide peaks and the sum integrated areas of oxide and carbonate peaks (denoted as $I_{Carbonate}/I_{Carbonate+Oxide}$) as a function of temperature to represent the relevant Li/O loss behavior. (c) Ni 2p XPS spectra for calcined NC91 samples at different temperatures; (d) The ratio of the integrated area of Ni(III) peak and the sum integrated area of Ni(III) and Ni(II) peaks (denoted as $I_{Ni(III)}/I_{Ni(III)+Ni(II)}$) as a function of temperature to represent the relevant O loss behavior.

(Fig. 2b). When the temperature is elevated to 300 °C (Fig. 4b), more spots are observed and indexed to higher-index planes $(-204)_L$ $(-108)_L$ and $(-20$ to $2)_L$ due to the evaporation of surface organic contamination. When the temperature is continuously raised to 500 and 700 °C (Fig. 4c and d), the spots belong to higher-index planes, gradually weaken and disappear, indicating the atomic disordering on the corresponding high-index planes. Different with XRD results above, the layered phase is still preserved even the temperature just reached 900 °C (Fig. 4e), which should be ascribed to the delay temperature response in the *in situ* TEM experiment. A swift and complete phase transformation from the layered phase to rock-salt phase is observed in the first 30 s at 900 °C in Fig. 4f. The interplanar spacings of $(006)_L$, $(-102)_L$ and $(104)_L$ are summarized in Fig. 4h as functions of temperature/time. The interplanar spacings of $(006)_L$ start to increase from 900 °C, indicating the starting of phase transformation and in consistent with the XRD results above. The spacings of $(-102)_L$ and $(104)_L$ keeps constant below 900 °C, then increases to the values of $(111)_R$ and $(-200)_R$ in rock-salt phase. This local observation of the phase transformation is consistent with the corresponding peak shifts in the Fig. 2**b**. In addition, the diffraction spots of layered phase and rock-salt phase are marked in the high resolution TEM images at 300 °C and after cooling down in Fig. 4i and j. Different with the above XRD analysis, CoO-type cubic phase is not observed here due to the very little phase content.

To further track the detailed phase transformation process, FFT is also performed for TEM images when holding at 900 °C (Fig. S7). As shown in Fig. 5, no obvious change happens in the very first 3 s. Then $(20-4)_L$ spots completely disappear, and $(006)_L$ spots become weak by the 5th second (Fig. 5c). $(006)_L$ spots continuously weaken and completely disappear by the 20th second in Fig. 5f, indicating the finish-up of the complete phase transformation within this single particle. The interplanar distances of $(-102)_L$, $(006)_L$ and $(104)_L$ are plotted in Fig. 5h as a function of time. The increase of their values is observed with time, which is consistent with the peak shifts in Fig. 2b. Different with the phase transformation in the bulk by XRD results, the local phase transformation within single particle is completed in just tens of seconds.

According to these observed results, the mechanism for the phase transformation is discussed here. As shown in Fig. 5i, the planes of $(-102)_L$, $(006)_L$ and $(104)_L$ are marked in the layered structure. It is clear, $(006)_L$ plane is composed with the ordered Li^+ ions in the Li layers. When Li^+ ions are gradually extracted from Li layers, $(006)_L$ spots will weaken and disappear. Both $(104)_L$ and $(-102)_L$ planes are constructed with TM cations and Li ions, it will transform into $(-200)_R$ and $(111)_R$ planes through Li/O loss and the merging of the neighboring TMO_6 layers (marked by two grey rectangles). On the whole, the phase transformation from the layered structure to the rock-salt structure is a smooth process involving Li/O loss and the merging of the adjacent TMO_6 layers, due to the great similarity of these two structures. That is why the phase transformation is not involving an amorphous intermediate.

To further analyze the phase transformation within single particle, we choose TEM image at 900 °C for the 10th second to do FFT in the bulk and at the surface of the selected single particle. As shown in Fig. 6a, the surface is still preserving the layered structure, but the bulk has completely transformed into the rock-salt phase. This interesting

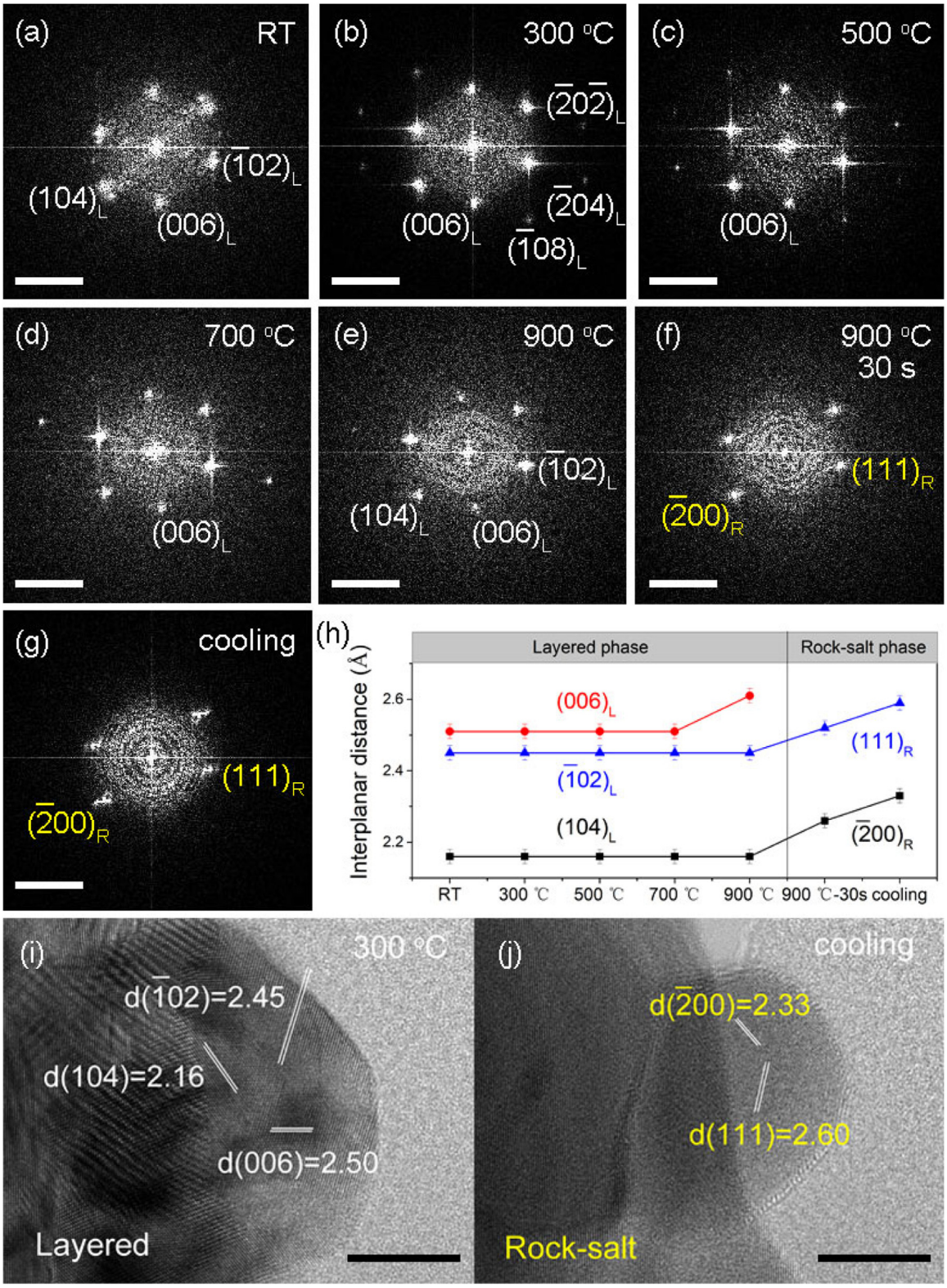

Fig. 4. Tracking the local structural evolution with temperature/time by FFT mapping. The FFT maps of the single particles in Fig. S6 at RT (a), 300 °C (b), 500 °C (c), 700 °C (d), 900 °C (e), 900 °C − 30 s (f), and after cooling down (g); (h) The interplanar distances of observed diffraction spots as a function of temperature; the indexing of observed lattice fringes for high resolution TEM images at 300 °C (i) and after cooling down (j). All the scale bars in the FFT maps are set as 5 1/nm, and the scale bars in the TEM images are set as 10 nm.

phenomenon has never reported before. To explain this phenomenon, a Li diffusion mechanism from the bulk to the surface is proposed here. As shown in Fig. 6b, the entire process could be divided into several steps: (1) layered phase at the surface initially decomposes into NiO-type rock-salt phase due to Li/O loss at the surface; (2) Li diffusion from the bulk to the surface is induced by the gradient of Li concentration between the surface and the bulk, which results into some low-Li/O areas in the bulk; (3) these low-Li/O areas transform to rock-salt phase in the

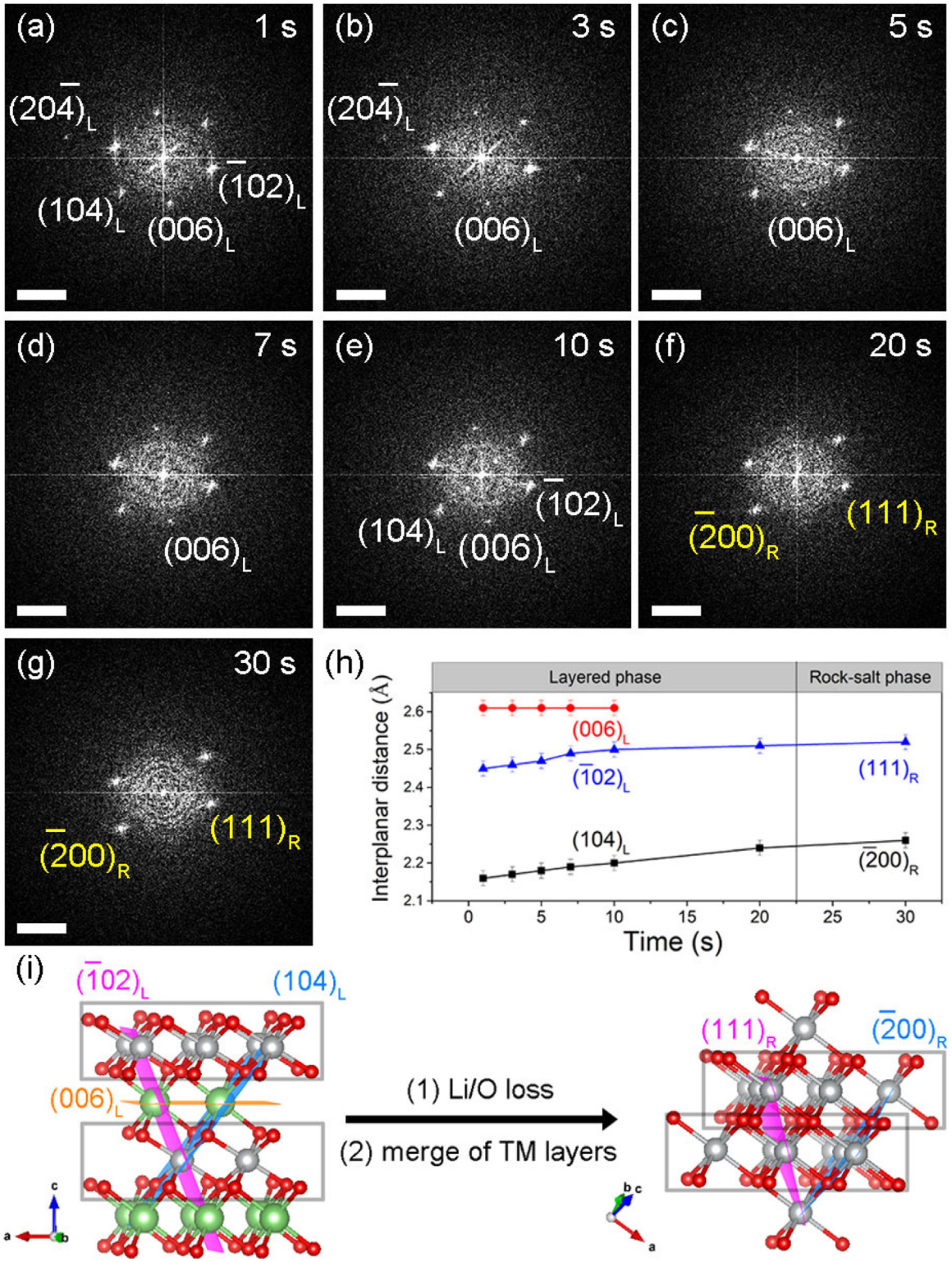

Fig. 5. Tracking the local structural evolution at 900 °C with time by FFT mapping. The FFT maps of the selected single particle when holding at 900 °C for 1 s (a), 3 s (b), 5 s (c), 7 s (d), 10 s (e), 20 s (f), and 30 s (g); (h) The interplanar distances of observed diffraction spots as a function of time; (i) The schematic illustration to show to the structural evolution from layered phase to rock-salt phase. All the scale bars in the FFT maps are set as 5 1/nm.

bulk with further Li/O loss; (4) these rock-salt areas grow and merge into larger rock-salt areas in the bulk; (5) when the rate of Li diffusion is comparable to the rate of Li/O loss at the surface at high temperatures, the phase transformation will spread from the bulk to the surface, and finally the entire particle will turn to rock-salt phase. This phase transformation process is very similar with that during the charging process of high-Ni layer oxides, and a similar “anti-core-shell” structure within single primary particles is observed here [32].

In brief, the whole phase transformation within single particles is induced by Li/O loss at the surface. Therefore, suppressing Li/O loss at the surface can efficiently suppress the phase transformation in the bulk. According to the previous reports, multiple strategies are adopted

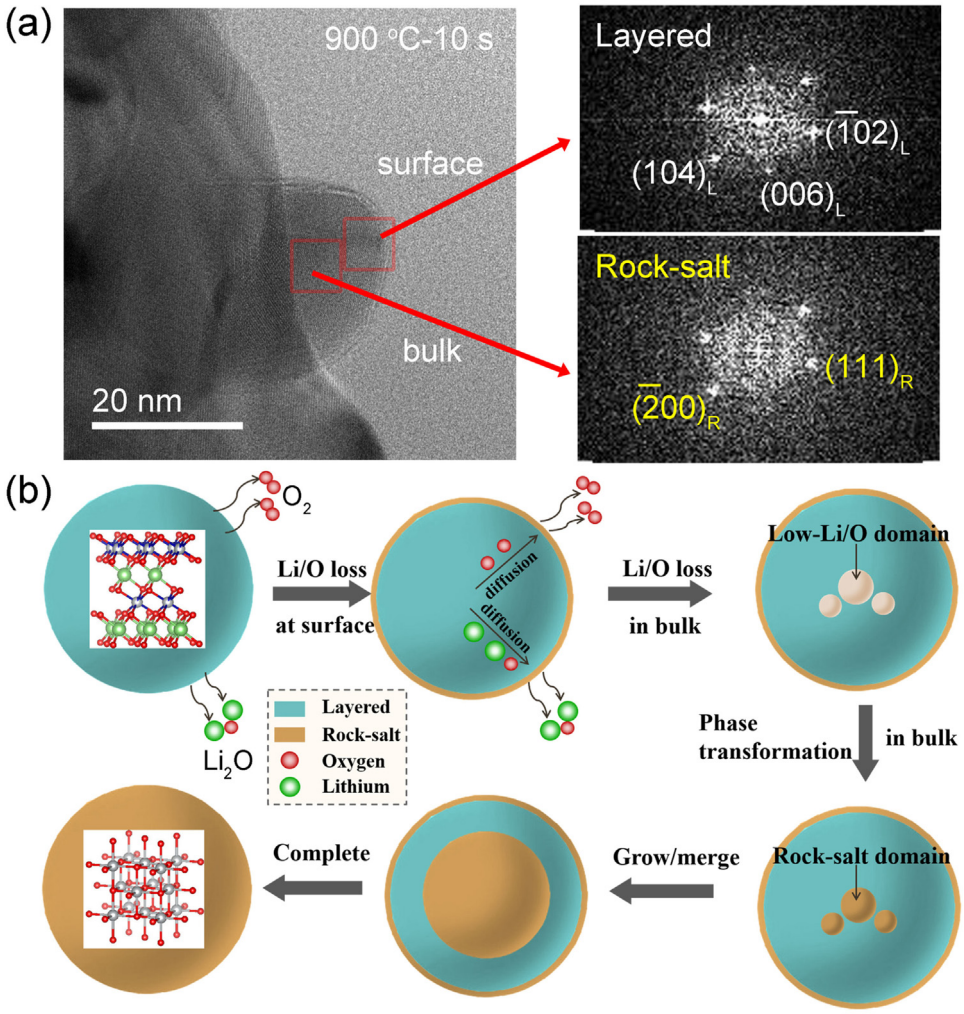

Fig. 6. The heterogenous phase transformation within single particle. (a) TEM image at 900 °C for the 10th second, as well as the FFT maps from the surface region and the bulk region (marked by red rectangles) within the selected single particle; (b) Schematic illustration to show the local phase transformation process within single particles.

to efficiently alleviate Li/O loss at the surface for enhancing the thermal/storage/cycling stability based on this mechanism, such as constructing Mn-rich surface by core-shell or concentration-gradient strategies [33,34], tailoring grain boundary structure [35], elemental surface doping (Ti, Zr, B) [36], surface coating with various inactive films, including Li_3PO_4 [37], Li_2SiO_3 [38], $Li_4Ti_5O_{12}$ [39], Al_2O_3 [40], etc.

3. Conclusions

In this work, multiple macroscopic/microscopic characterization techniques, including *in-situ time/temperature-resolved* TEM, *ex-situ* XRD, and XPS, are combined to comprehensively investigate the thermal-induced phase transformation process involving Li/O loss in a representative binary high-Ni layered oxide $LiNi_{0.9}Co_{0.1}O_2$. Based on a Li/O loss model, namely $[Li_{1-x}Ni_x]_{3b}[Ni_{0.9-x}Co_{0.1}]_{3a}O_{2-x}$, the whole process of Li/O loss is quantitatively tracked from the bulk and the surface during the phase transformation, hinting the heterogeneous Li/O loss in the bulk and at the surface. Especially, when Li/O loss approach to 20–30%, the layered structure becomes instable and transforms to rock-salt phase $Li_{1-x}Ni_xO$ ($x \sim 80\%$) at high temperature accompanying with serious Li/O loss. *In situ* TEM studies in single primary particles further reveal an anti-core-shell intermediate during the calcination. It indicates, Li/O loss in the bulk is induced by that at the surface, resulting into a rock-salt phase *via* the high Li diffusivity at high temperature. It further highlights the importance of surface protection within the primary particles, which could greatly hinder Li/O loss at the surface and thereby alleviate the phase transformation in the bulk. The quantitative analysis and direct observations herein not only demonstrate a feasible route to study the Li/O loss behaviors, but also provide valuable insights into the improvement of the thermal stability and cycling stability from the aspect of Li/O loss.

Acknowledgments

This work was supported by the Guangdong Innovative Team Program (2013N080), Guangdong Key-lab Project (No. 2017B0303010130), the Peacock Plan (KYPT20141016105435850), Shenzhen Science and Technology Research Grant (ZDSYS201707281026184), China Postdoctoral Science Foundation (2015M570882, 2015M570894), the International Postdoctoral Exchange Fellowship Program (No. 53 Document of OCPC, 2016).

Notes

The authors declare no competing financial interests.

Appendix A. Supporting information

Supplementary data associated with this article can be found in the online version at doi:10.1016/j.nanoen.2019.02.059.

References

[1] J. Lu, Z.H. Chen, Z.F. Ma, F. Pan, L.A. Curtiss, K. Amine, Nat. Nanotechnol. 11 (2016) 1031–1038.
[2] Z.Z. Wu, S.P. Ji, J.X. Zheng, Z.X. Hu, S. Xiao, Y. Wei, Z.Q. Zhuo, Y. Lin, W.L. Yang, K. Xu, K. Amine, F. Pan, Nano Lett. 15 (2015) 5590–5596.
[3] B.B. Lim, S.J. Yoon, K.J. Park, C.S. Yoon, S.J. Kim, J.J. Lee, Y.K. Sun, Adv. Funct. Mater. 25 (2015) 4673–4680.
[4] D. Wang, R. Kou, Y. Ren, C.J. Sun, H. Zhao, M.J. Zhang, Y. Li, A. Huq, J.Y.P. Ko, F. Pan, Y.K. Sun, Y. Yang, K. Amine, J. Bai, Z. Chen, F. Wang, Adv. Mater. 29 (2017) 1606715.
[5] J.Q. Zhao, W. Zhang, A. Huq, S.T. Misture, B.L. Zhang, S.M. Guo, L.J. Wu, Y.M. Zhu, Z.H. Chen, K. Amine, F. Pan, J.M. Bai, F. Wang, Adv. Energy Mater. 7 (2017) 1601266.
[6] J. Li, H.S. Liu, J. Xia, A.R. Cameron, M.Y. Nie, G.A. Botton, J.R. Dahn, J. Electrochem. Soc. 164 (2017) A655–A665.
[7] W.D. Qiu, J. Xia, L.P. Chen, J.R. Dahn, J. Power Sources 318 (2016) 228–234.
[8] J. Li, L.E. Downie, L. Ma, W.D. Qiu, J.R. Dahn, J. Electrochem. Soc. 162 (2015) A1401–A1408.
[9] P.F. Zhou, H.J. Meng, Z. Zhang, C.C. Chen, Y.Y. Lu, J. Cao, F.Y. Cheng, J. Chen, J. Mater. Chem. A 5 (2017) 2724–2731.
[10] C.S. Yoon, H.H. Ryu, G.T. Park, J.H. Kim, K.H. Kim, Y.K. Sun, J. Mater. Chem. A 6 (2018) 4126–4132.
[11] P.-C. Tsai, B. Wen, M. Wolfman, M.-J. Choe, M.S. Pan, L. Su, K. Thornton, J. Cabana, Y.-M. Chiang, Energy Environ. Sci. 11 (2018) 860–871.
[12] W. Lee, S. Muhammad, T. Kim, H. Kim, E. Lee, M. Jeong, S. Son, J.H. Ryou, W.S. Yoon, Adv. Energy Mater. 8 (2018).
[13] H.H. Ryu, K.J. Park, C.S. Yoon, Y.K. Sun, Chem. Mater. 30 (2018) 1155–1163.
[14] Y. Xia, J.M. Zheng, C.M. Wang, M. Gu, Nano Energy 49 (2018) 434–452.
[15] I.A. Shkrob, J.A. Gilbert, P.J. Phillips, R. Klie, R.T. Haasch, J. Bareno, D.P. Abraham, J. Electrochem. Soc. 164 (2017) A1489–A1498.
[16] H.S. Liu, Y. Yang, J.J. Zhang, J. Power Sources 173 (2007) 556–561.
[17] Y. Koyama, T. Mizoguchi, H. Ikeno, I. Tanaka, J. Phys. Chem. B 109 (2005) 10749–10755.
[18] S.K. Jung, H. Gwon, J. Hong, K.Y. Park, D.H. Seo, H. Kim, J. Hyun, W. Yang, K. Kang, Adv. Energy Mater. 4 (2014) 1300787.
[19] W. Zhao, J. Zheng, L. Zou, H. Jia, B. Liu, H. Wang, M.H. Engelhard, C. Wang, W. Xu, Y. Yang, J.-G. Zhang, Adv. Energy Mater. (2018) 1800297.
[20] X.H. Liu, L.Q. Kou, T. Shi, K. Liu, L. Chen, J. Power Sources 267 (2014) 874–880.
[21] P. Dong, D. Wang, Y. Yao, X. Li, Y.J. Zhang, J.J. Ru, T. Ren, J. Power Sources 344 (2017) 111–118.
[22] P.G. Balakrishnan, R. Ramesh, T.P. Kumar, J. Power Sources 155 (2006) 401–414.
[23] L.G. Lu, X.B. Han, J.Q. Li, J.F. Hua, M.G. Ouyang, J. Power Sources 226 (2013) 272–288.
[24] J.B. Goodenough, D.G. Wickham, W.J. Croft, J. Phys. Chem. Solids 5 (1958) 107–116.
[25] J. Lee, A. Urban, X. Li, D. Su, G. Hautier, G. Ceder, Science 343 (2014) 519–522.
[26] Y. You, H. Celio, J.Y. Li, A. Dolocan, A. Manthiram, Angew. Chem.-Int. Ed. 57 (2018) 6480–6485.
[27] Y. Li, R. Xu, Y. Ren, J. Lu, H.M. Wu, L.F. Wang, D.J. Miller, Y.K. Sun, K. Amine, Z.H. Chen, Nano Energy 19 (2016) 522–531.
[28] S.M. Bak, E.Y. Hu, Y.N. Zhou, X.Q. Yu, S.D. Senanayake, S.J. Cho, K.B. Kim, K.Y. Chung, X.Q. Yang, K.W. Nam, ACS Appl. Mater. Interfaces 6 (2014) 22594–22601.
[29] S.T. Myung, F. Maglia, K.J. Park, C.S. Yoon, P. Lamp, S.J. Kim, Y.K. Sun, ACS Energy Lett. 2 (2017) 196–223.
[30] H.J. Noh, S. Youn, C.S. Yoon, Y.K. Sun, J. Power Sources 233 (2013) 121–130.
[31] C.H. Jo, D.H. Cho, H.J. Noh, H. Yashiro, Y.K. Sun, S.T. Myung, Nano Res. 8 (2015) 1464–1479.
[32] H. Zhang, F. Omenya, M.S. Whittingham, C. Wang, G. Zhou, ACS Energy Lett. 2 (2017) 2598–2606.
[33] Y.K. Sun, S.T. Myung, B.C. Park, J. Prakash, I. Belharouak, K. Amine, Nat. Mater. 8 (2009) 320–324.
[34] Y.K. Sun, Z.H. Chen, H.J. Noh, D.J. Lee, H.G. Jung, Y. Ren, S. Wang, C.S. Yoon, S.T. Myung, K. Amine, Nat. Mater. 11 (2012) 942–947.
[35] P.F. Yan, J.M. Zheng, J. Liu, B.Q. Wang, X.P. Cheng, Y.F. Zhang, X.L. Sun, C.M. Wang, J.G. Zhang, Nat. Energy 3 (2018) 600–605.
[36] F. Schipper, M. Dixit, D. Kovacheva, M. Talianker, O. Haik, J. Grinblat, E.M. Erickson, C. Ghanty, D.T. Major, B. Markovsky, D. Aurbach, J. Mater. Chem. A 4 (2016) 16073–16084.
[37] S.W. Lee, M.S. Kim, J.H. Jeong, D.H. Kim, K.Y. Chung, K.C. Roh, K.B. Kim, J. Power Sources 360 (2017) 206–214.
[38] E.Y. Zhao, M.M. Chen, Z.B. Hu, D.F. Chen, L.M. Yang, X.L. Xiao, J. Power Sources 343 (2017) 345–353.
[39] Y.D. Xu, W. Xiang, Z.G. Wu, C.L. Xu, Y.C. Li, X.D. Guo, G.P. Lv, X. Peng, B.H. Zhong, Electrochim. Acta 268 (2018) 358–365.
[40] K. Du, H.B. Xie, G.R. Hu, Z.D. Peng, Y.B. Cao, F. Yu, ACS Appl. Mater. Interfaces 8 (2016) 17713–17720.